

NASA TECHNICAL NOTE



NASA TN D-2050

C-1

NASA TN D-2050

LOAN COPY: R
AFWL (W)
KIRTLAND AFB



**EFFECTS OF FLANK LOSSES IN THE
THEORY OF SPACE-PROBE ENTRY
UNDER CONDITIONS OF HIGH MASS LOSS**

by Frederick C. Grant

*Langley Research Center
Langley Station, Hampton, Va.*

TECH LIBRARY KAFB, NM



0154520

TECHNICAL NOTE D-2050

EFFECTS OF FLANK LOSSES IN THE THEORY OF SPACE-PROBE ENTRY
UNDER CONDITIONS OF HIGH MASS LOSS

By Frederick C. Grant

Langley Research Center
Langley Station, Hampton, Va.

NATIONAL AERONAUTICS AND SPACE ADMINISTRATION

THE ECHO I INFLATION SYSTEM

By Dewey L. Clemmons, Jr.

SUMMARY

A study has been made to determine the feasibility and selection of a subliming compound to be used as an inflation system for the Echo I satellite. Primary considerations have been given to the compatibility of such a system with payload weight limitations, storage in satellite, internal pressure requirements, and the minimum length of time that the inflation need be sustained. Calculations are made to determine the temperature variations of the satellite while in sunlight and shadow, the deforming loads present in the environment of space, the effects of micrometeoroids with regard to holes punctured in the satellite, the method of selecting the proper subliming compound as well as the pressure time history and mass flow rate of the inflation vapors.

It can be generalized from this investigation that subliming organic compounds lend themselves very well to the initial inflation of large, thin wall, spherical configurations in orbit above the earth's atmosphere and pressure sustenance can be achieved for periods of the order of a few weeks. In particular, it was found for the Echo I satellite that (1) the thermal response would be so rapid that a continuous sunlight orbit would be required for the subliming compound to achieve maximum performance, (2) the maximum deforming loads would result from the satellite's memory of its original folded configuration, (3) micrometeoroid hole area would be produced at the rate of about 28.1 square centimeters per day, and (4) the inflation and pressure sustenance requirement would be satisfied with 4.54 kilograms of benzoic acid and 9.18 kilograms of anthraquinone to maintain a pressure of about 10^{-3} torr for about 13 days for evaluation of the satellite as a passive communications relay station.

A comparison between the predicted performance of the inflation system and that inferred by experimental scattering of microwave signals by the satellite is discussed. The referenced experimental evidence indicates that the sphericity of the satellite began to degrade after a period of 6 to 12 days after launch.

INTRODUCTION

The Echo I satellite was designed as an experimental, spherical, passive radio relay station to be placed in a circular orbit around the earth for the purpose of evaluation as a means of increasing worldwide communications. The advantages of such a satellite are that it permits the extension of the usable radio-frequency spectrum for long-range communications between points on the

earth, as well as providing continuous surface coverage over the range of mutual visibility for transmitting and receiving stations. The frequency spectrum is extended by reflecting signals back to the earth that are of sufficiently high frequency to penetrate the ionosphere. The surface coverage is increased by virtue of the fact that the spherical reflector is an isotropic scatterer of electromagnetic radiation that will permit signal reception at all points on the earth's surface that are geometrically visible from the satellite. This is an improvement over the method of radio communication over long ranges by reflecting signals off the ionosphere where large voids remain in surface coverage between the points where the signal is reflected from the earth and ionosphere.

The spherical shape of the satellite is advantageous for a number of reasons: (1) its spherical symmetry eliminates the need for any orientation control, (2) it permits the development of high stresses in the skin by an inflation gas without the occurrence of stress concentrations that would have to be reinforced by weight penalizing materials, and (3) the previously mentioned isotropic scattering characteristic that affords equal opportunity for all stations to use the satellite as long as it remains mutually visible to sender and receiver. Since the satellite acts as a passive relay station, it has the capability of reflecting all frequencies simultaneously and eliminating frequency channel restrictions that would be imposed by an active repeater.

It was determined that a satellite 30.48 meters (100 feet) in diameter would be compatible with presently existing research transmitting facilities in relaying voice communications over the range involved while maintaining sufficient signal strength to be received at the receiving stations. The large sphere was designed to be placed in a circular orbit 1668 kilometers above the earth's surface. In keeping with the payload weight and size limitations imposed by the launching vehicle, it was required that the folded sphere and its inflation system weigh only 68 kilograms and fit inside a spherical container only 67 centimeters in diameter. The inflation compounds weighed 13.6 kilograms. Once the payload was injected into orbit, it was programmed to be separated from the last-stage spent rocket motor by a spring-loaded mechanism. After a sufficient time had elapsed for a separation distance of approximately 60 meters to exist between the rocket motor and payload container, the two container hemispheres were accelerated away from each other by means of an explosive charge.

While conforming with the weight requirements, the inflation system was required to erect the folded configuration to a spherical shape and stress the skin so that no irregularities would remain that would distort the incident radio signals and maintain a minimum internal pressure for the 1- to 2-week test period necessary to evaluate the satellite as a passive radio relay station.

Before this experiment there had never been an attempt to erect such a large, thin-wall structure in space. In the past, conventional methods utilizing bottled, compressed gas had been satisfactory for smaller, thicker walled, inflatable satellites where weight and storage of necessary quantities were not of prime consideration. In this application consideration was given

to several aspects of the gas bottle method which included: (1) the weight of the bottles required to store sufficient quantities of gas to erect and sustain the pressure during the test period, (2) the complications arising from attempts to store the bottle with the compactly folded satellite, (3) the danger of the gas leaking from the bottles during payload storage and transit that would cause the satellite to virtually explode when released in the vacuum of space and, (4) the complications involved in a method to actuate gas injection into the satellite at the proper time and at the proper rate. The obvious problems associated with these considerations leave a great deal to be desired in this method of inflation. A novel concept conceived for the Echo I inflation was based on the principle of subliming compounds that could be distributed throughout the inside of the sphere in a loose powder form in such a manner that it lends itself to the folding and packaging technique. The powders must be of such character that they can be induced to liberate vapors for erecting and maintaining inflation once the satellite is in orbit.

The purpose of this paper is to present an analysis of the factors affecting the erection and pressure sustenance of the Echo I satellite by using the sublimation principle and to show, from this analysis, a method of selecting subliming compounds that will meet the requirements previously stated. Details are presented with regard to the dynamic thermal response of the satellite, deforming loads, effects of micrometeoroids, selection of subliming compounds, pressure time history inside the satellite, and the rate of mass flow of vapors out of the satellite as a result of leakage.

SYMBOLS

A	area, cm^2
A'	thermodynamic constant, dimensionless
a	earth's albedo, assumed 0.36
B'	thermodynamic constant, $^{\circ}\text{K}^{-1}$
C'	a simplifying collection of terms, $3.64 \times 10^3 \sqrt{\frac{T}{MV^2}}, \text{cm}^{-2}\text{-sec}^{-1}$
C _S	solar radiation constant, $1.3953 \times 10^6 \text{ ergs-sec}^{-1}\text{-cm}^{-2}$
c	velocity of light in vacuo, $2.99776 \times 10^{10} \text{ cm-sec}^{-1}$
c'	constant of integration, dynes-cm^{-2}
c _p	specific heat of the form $y^2 + z^2T$, $\text{erg-gm}^{-1}\text{-}^{\circ}\text{K}^{-1}$
D	diameter, cm

d	depth of penetration, cm
dm/dt	mass flow rate, gm-sec ⁻¹
dq/dt	heat flow rate, erg-sec ⁻¹
$d\bar{T}/dt$	average temperature change rate, °K-sec ⁻¹
E	modulus of elasticity, dynes-cm ⁻²
F_R	geometric view factor, dimensionless
f	air orifice hole size, cm ²
g	rate of micrometeoroid hole growth, cm ² -sec ⁻¹
g_0	gravitational acceleration at earth's surface, 9.814×10^2 cm-sec ⁻²
h	satellite altitude, cm
I	influx, micrometeoroids-sec ⁻¹
j	ratio of microscopic surface to apparent surface area, dimensionless
E_k	kinetic energy, ergs
k	$\frac{R_E}{R_E + h}$, dimensionless
k'	Boltzmann's constant, 1.3803×10^{-16} ergs-molecule ⁻¹ -°K ⁻¹
M	molecular weight, gm-(gm-mole) ⁻¹
m	mass, gm
N	number of molecules, molecules
N_g	Avogadro's number, 6.025×10^{23} molecules-(gm-mole) ⁻¹
n	number molecular density, molecules-cm ⁻³
p	pressure, dynes-cm ⁻²
q	thermal energy, ergs
R	radius, cm
R_g	universal gas constant, 8.3149×10^7 ergs-(gm-mole) ⁻¹ -°K ⁻¹

heat-protection material. A payload is attached at the rear of the probe. The lowest entry velocity for which the entire volume of heat-protection material is consumed is defined as the limiting velocity. It is evident that the change in the mass and drag of the vehicle introduced by the flank losses will have an effect on the limiting velocity.

The heat-input function, from equation (2b) of reference 1, has the form

$$q = (\text{Constant}) \rho^r U^s g(\lambda) \quad (1)$$

where q is the heat transfer per unit area, ρ is the ambient air density, U is the vehicle velocity, and $g(\lambda)$ is a function of the shape. The probe is considered to enter the atmosphere at a speed so high that a single term with the form of the right-hand side of equation (1) can be used to represent the heat input which is dominated by radiative transfer at the high speeds to be considered.

In reference 1 the following special choice of parameters was made in the general form given by equation (1):

$$r = 1$$

$$s = 3$$

$$(\text{Constant}) g(\lambda) = \frac{\eta}{2}$$

so that the heat-input function has the form

$$q = \eta \frac{\rho}{2} U^3 \quad (2)$$

Equation (2) expresses the heat input per unit area of the face as a fraction η of the flux of kinetic energy of the flow. The fraction η is in reality not constant but depends on ρ , U , and the geometry of the body. The quantity η is to be treated as a constant in the present analysis which means that it represents an effective value typical of conditions during the high-mass-loss pulse. Values of η are indicated in reference 2 for a wide range of values of ρ , U , and shock standoff distance.

The motion equation used was

$$-m\dot{U} = \frac{1}{2} C_D A \rho U^2 \quad (3a)$$

in which gravity is neglected and the vaporized probe material is assumed to leave with zero velocity with respect to the probe. The velocities considered are so high that during the time of high deceleration and high mass-loss rate the trajectory may be approximated as a straight line. Equation (3a) may be written as

$$-\frac{dU}{d\rho} = f(\lambda)U \quad (3b)$$

By combination of the equation of motion with the heating relation (eq. (1)) the following equation for the size as a function of altitude was derived as equation (3c) of reference 1

$$\frac{d^2\lambda}{d\omega^2} + \left[(s-1)e^{\omega}f(\lambda) - r \right] \frac{d\lambda}{d\omega} - \frac{g'(\lambda)}{g(\lambda)} \left(\frac{d\lambda}{d\omega} \right)^2 = 0 \quad (4a)$$

where λ is the nondimensional length and $\omega = \log_e \rho$ where ρ is the air density. The variable ω is proportional to the altitude in the assumed isothermal atmosphere at constant acceleration of gravity. Solutions of equation (4a) are related to the velocity through the slope of the integral curves by

$$-\frac{d\lambda}{d\omega} = e^{r\omega} U^{s-1} g(\lambda) \geq 0 \quad (4b)$$

The ballistic function $f(\lambda)$ which occurs in equations (3b) and (4a) is given by

$$f(\lambda) = \frac{a_g h_s'}{2\delta}$$

where $\delta = ma_g/C_D A$ is the ballistic parameter and h_s' is the generalized scale height

$$h_s' = \frac{h_s}{\sin \gamma}$$

where γ is the angle of the flight path with respect to the horizontal and h_s is the scale height

$$h_s = - \frac{dh}{d \log_e \rho}$$

which is presumed constant. A prime concern of the present analysis is to evaluate the influence on limiting velocity of the functions $f(\lambda)$ which are appropriate to the case of finite mass loss on the flanks.

If an expression similar to equation (2) is written for the heat input to the flanks the heat input per unit area is found to be

$$q_f = \eta_f \frac{\rho}{2} U^3 \sin^3 \theta_c \quad (5)$$

The velocity used in equation (2) to obtain equation (5) is the component of free-stream velocity normal to the flanks. Because of the assumed uniformity of the different rates of ablation on the flanks and the face the blunted cone will remain a blunted cone. The mass loss on the flanks will tend to decrease the size of the face and the mass loss on the face will tend to increase the size of the face. Equation of the heat capacity of the material to the heat inputs on the face yields

$$-\Delta W \dot{w}_x = \eta \frac{\rho}{2} U^3$$

and on the flanks yields

$$-\Delta W \dot{w}_y = \eta_f \frac{\rho}{2} U^3 \sin^3 \theta_c$$

so that

$$\frac{dy}{dx} = \epsilon \sin^3 \theta_c$$

where

$$\epsilon = \frac{\eta_f}{\eta}$$

If the face size is held constant then

$$\frac{dy}{dx} = \sin \theta_c = \epsilon \sin^3 \theta_c$$

or

$$\epsilon = 1 + \left(\frac{2L}{D} \right)^2 \geq 1 \quad (6a)$$

Relation (6a) suggests that the face must always grow since the weaker shock strength on the swept flanks implies that the reversed inequality

$$\epsilon \leq 1 \quad (6b)$$

actually holds. The results of reference 2 indicate that the inequality (6b) does hold nearly everywhere in the ρU -plane.

Even for quite blunt cones the heat transfer to the flanks, as measured by η_F , must greatly exceed that to the face if the face is not to grow. The relative size of η_F and η will be discussed subsequently.

It was shown in reference 1 that the limiting velocity U_l is given by

$$U_l^2 = \frac{\Delta W}{\eta} \frac{2wL}{h_s'} F(\lambda_{\infty-}) \quad (7)$$

for heat inputs of the type defined by equation (2) where

$$F(\lambda) = 2 \int_0^\lambda f(\lambda) d\lambda \quad (8)$$

The function $f(\lambda)$ depends on the parameter ϵ in a way which is indicated in the following discussion. Because the probe remains in the class of truncated cones even with mass loss on the flanks, the ballistic function $f(\lambda)$ may be evaluated for the cone with mass loss on the flanks in terms of the function $f(\lambda)$ for the cone with mass loss only on the face. Appropriate changes must be made in the length parameter L and the payload-fraction parameter μ . The ablation on the flanks continuously reduces the length parameter L and increases the payload-fraction parameter μ . Rewriting the $\eta = 0$ function, equation (4c) of reference 1, by priming the quantities λ , L except in $D/2L$, and μ gives for $\eta_F > 0$

$$f(\lambda') = 3 \frac{gh_s'}{wL} \frac{\frac{L}{L'}}{\frac{1}{1-\mu'} - (1-\lambda')^3 - \frac{\mu'}{1-\mu'}(1-\lambda_{\infty-})^3} \frac{(1-\lambda')^2 + \left(\frac{D}{2L}\right)^2}{1 + \left(\frac{D}{2L}\right)^2} \quad (9)$$

The right-hand side of equation (9) is to be used for the function $f(\lambda)$ in the integral of equation (8). The primed variables of equation (9) must be related to the variable of integration λ which is based on the fixed unit of length L .

The primed nondimensional length is expressed as

$$\lambda' = \left(\frac{L}{L'}\right)\lambda$$

where the variable

$$\lambda = \frac{l}{L}$$

The size-parameter ratio is given by

$$\frac{L}{L'} = \left[1 - \tau(\lambda_{\infty} - \lambda) \right]^{-1}$$

for

$$\tau = \frac{\epsilon}{1 + \left(\frac{2L}{D} \right)^2}$$

and the new payload-fraction parameter μ' is given by

$$\frac{\mu'}{1 - \mu'} = \frac{\mu}{1 - \mu} \left(\frac{L}{L'} \right)^3$$

Although $f(\lambda)$ as given by equation (9) is, as the quotient of two polynomials, integrable in terms of elementary functions, the integrations required for evaluation of $F(\lambda)$ will, for convenience, be performed numerically.

The integral $F(\lambda_{\infty})$ depends parametrically on μ , ϵ , and D/L . In reference 1 the restriction of $\epsilon = 0$ implied that only the smaller values of D/L could be considered. With the introduction of finite values of ϵ the whole range of values of D/L is open to examination. The calculations which are to be presented will show the limiting velocity to be a monotonic increasing function of the cone angle for a given value of ϵ and a monotonic decreasing function of the rate of heat transfer to the flanks as measured by η_f .

As η_f increases from zero to η (or as ϵ approaches 1) an interesting limit appears. When $\eta_f = \eta$ and $\lambda_{\infty} = 1$

$$\tau = \frac{a}{1 + a} \quad 1 - \tau = \frac{1}{1 + a}$$

for

$$a = \left(\frac{D}{2L} \right)^2$$

and

$$U_l^2 = 12a_g \left(\frac{\Delta W}{\eta} \right) I(a)$$

where

$$I(a) = \int_0^1 \frac{1}{1 - u^3 + \frac{\mu}{1 - \mu}(1 + au)^3} \frac{u^2 + a}{1 + au} du \quad (10)$$

for

$$u = 1 - \lambda'$$

On the substitution of

$$t = \frac{1 - u}{1 + au}$$

in equation (10) it is found that

$$I(a) = \frac{1}{3} \left\{ \log_e \left[(1 + at)^3 - (1 - t)^3 + \frac{\mu}{1 - \mu}(1 + a)^3 \right] \right\}_0^1 = \frac{1}{3} \log_e \frac{1}{\mu}$$

The limiting speed is thus independent of the cone angle so that all the cones have the same limiting speed, that of a cylinder, with zero flank loss, which is given by

$$U_l^2 = 4a_g \left(\frac{\Delta W}{\eta} \right) \log_e \frac{1}{\mu} \quad (11)$$

The case $\eta_f = \eta$ thus marks the boundary for gains in limiting speed due to increasing the cone angle. For $\eta_f < \eta$ improvement on the limiting speed of a cylinder by increasing the cone angle is possible.

Whether the desired low value of η_f on the flanks is likely to exist requires investigation. It may be most conveniently discussed in terms of a velocity-altitude diagram such as that of figure 2.

The appearance of the lines of constant η as indicated by the normal shock results of reference 2 is sketched in figure 2. The form and position of the

contour lines are different for different values of standoff distance and figure 2 is intended only as a qualitative sketch. The discussion assumes that the velocities are high enough that the dominant mode of heat transfer to the body is through radiation.

Consider a trajectory for which the point 1 of figure 2 is typical of conditions at the peak-heating-rate condition. Although the indications of figure 2 are for normal shocks, the conditions on the flanks of the cone are roughly those behind a normal shock at a velocity equal to the normal component of the vehicle velocity so that the value of η_f may be found by moving to lower velocities in figure 2 without changing altitude. The velocity equivalence is expressed by

$$U_f = U \sin \theta_c$$

It may be seen immediately that for the face condition 1 in figure 2 a sweep angle sufficient to put the flank normal velocity at point 2 does not change η_f whereas further sweep to point 3 does lower η_f . For a smaller vehicle with the typical peak heating condition 1' the same amount of sweep as moved the effective velocity to point 2 without changing η_f now does lower η_f .

In general, the possibility of gains in limiting velocity by steepening of the flanks depends on the position of the high-mass-loss region in the velocity-altitude plane. For the largest vehicles and highest velocities there seems to be a limited possibility of achieving higher limiting velocities by means of flank steepening. Such vehicles are characterized by high-mass-loss regions with the typical point 1. For many other positions such as point 1' there is a greater possibility of improvement in limiting velocity or, alternatively, of higher payload fractions. Quantitative analysis of the possibilities will not be attempted in this paper.

Probes With Curved Meridians

The fact that for sufficiently low values of η_f the cone offers an improvement on the cylinder suggests that a second-degree variation of radius with axial distance may offer an improvement on the cone. (See fig. 3.) The use of a vehicle with a cusped nose was suggested on page 265 of reference 3 under conditions of low mass loss. Immediate difficulties appear in attempting an analysis of second-order radius variation on the same level of approximation as for the cylinder and the cone which correspond to zero and first-order radius variations, respectively. In the first place, it can be shown that a probe with a second-order variation of radius along the axis will not retain a second-order variation for the type of flank heat input previously used (eq. (5)). In the second place, the fact that the slope is different at each axial station means that the effect of sweep angle appears in establishing the effective value of η_f . An averaging over slopes is thus required which lowers the level of approximation of the analysis. Accordingly, only the simplest case will be considered. The simplest case

is that of $\eta_F = 0$ for the limit of steep slopes $D/L = \infty$. The results to be obtained may be regarded as yielding a crude indication of the effects of axial mass distribution of the heat-protection material for idealized and very favorable conditions.

A section through the axis of an axisymmetric probe with curved meridians is given in figure 3. The shape of the curved meridian has the form

$$\frac{d}{2} = (1 - \lambda)^n \frac{D}{2}$$

where the nondimensional length is

$$\lambda = \frac{x}{L}$$

The limiting velocity U_l is given by equation (7) rewritten as

$$U_l^2 = 2a_g \left(\frac{\Delta W}{\eta} \right) W L \int_0^{\lambda_{\infty}} \delta^{-1} d\lambda \quad (12)$$

with the ballistic parameter given by

$$\delta = \frac{ma_g}{C_D A}$$

If the value of D/L is assumed to be large enough that $C_D A$ can be replaced in the integral by

$$\frac{\pi D^2}{2}$$

equation (12) becomes

$$U_l^2 = 2a_g \left(\frac{\Delta W}{\eta} \right) W L \frac{\pi D^2}{2} \int_0^1 \frac{d\lambda}{ma_g} \quad (13)$$

where the upper limit has been given its maximum value to maximize the integral. The limiting velocity thus depends, in this extreme case, only on the axial weight distribution, that is, on ma_g as a function of λ .

For the probes in figure 3 the weight is found to be

$$ma_g = \frac{wL}{2n+1} \frac{\pi D^2}{4} \left\{ \left[1 - (1 - \lambda)^{2n+1} \right] + \frac{\mu}{1 - \mu} \left[1 - (1 - \lambda_{\infty})^{2n+1} \right] \right\} \quad (14)$$

where μ is the payload fraction. Inserting equation (14) into equation (13) and changing the variable to $z = \frac{1 - \lambda}{c}$ gives

$$U_l^2 = 4a_g \left(\frac{\Delta W}{\eta} \right) \frac{2n+1}{c^{2n}} \int_0^{c^{-1}} \frac{dz}{1 - z^{2n+1}} \quad (15)$$

where

$$c^{2n+1} = \frac{1}{1 - \mu}$$

If the limiting velocity of a cylinder ($n = 0$) is taken as the unit, the velocity R is given by

$$R^2 = \frac{2n+1}{\log_e \frac{1}{\mu}} \frac{1}{c^{2n}} \int_0^{c^{-1}} \frac{dz}{1 - z^{2n+1}} \quad (16)$$

When the denominator of the integrand of equation (16) is always given its maximum value, unity, a lower bound on R is established as

$$R^2 \geq \frac{(2n+1)(1-\mu)}{\log_e \frac{1}{\mu}}$$

Thus R^2 increases to infinity with n . The integrals of equation (15) are evaluated in the appendix.

NUMERICAL RESULTS

Cones With Flank Losses

The value of limiting velocity for cylinders ($D/L = 0$) was indicated previously in equation (11), which is

$$U_l^2 = 4a_g \left(\frac{\Delta W}{\eta} \right) \log_e \frac{1}{\mu}$$

In presenting results for the cones with ablating flanks, the value of U_l indicated by equation (11) will be used as a unit. This normalization of U_l has the advantage of yielding a result which is independent of $\Delta W/\eta$. Values of U_l , as indicated by equation (11), for $\mu = 1/e$ are given in figure 4. To obtain values of U_l for other values of μ , the value of U_l obtained from figure 4 for the proper value of $\Delta W/\eta$ should be multiplied by

$$\sqrt{\log_e \frac{1}{\mu}}$$

In units of the cylinder velocities indicated by figure 4, the limiting velocity R for cones with different half-angles and rates of flank loss are indicated in figure 5 for four values of μ . The quantity ϵ is defined as

$$\epsilon = \frac{\eta_f}{\eta}$$

and the limiting velocity is expressed as

$$(U_l)_{\epsilon, \theta_c} = R(U_l)_{cyl}$$

where $(U_l)_{cyl}$ is given in figure 4. The dependency of R on μ is not (except for $\epsilon = 1$) separable as is the dependency of U_l on μ for the cylindrical shape. Hence a separate, but similar, set of curves is required for each value of μ . The curves of figure 5 are monotonic, increasing with θ_c so that peak R occurs for $\theta_c = 90^\circ$. It should be realized, however, that ϵ increases with θ_c in real cases as the shock strength on the flanks increases with θ_c and approaches that of a normal shock for $\theta_c = 90^\circ$. Thus the peak R will occur for each μ and size at a cone half-angle less than 90° . A qualitative idea of the sort of variation to be expected is sketched as a dashed line in figure 5(a). The values of R corresponding to a cone half-angle of 90° have the character of absolute upper bounds, however, and are indicated in the following table for convenience:

μ	R for $\theta_c = 90^\circ$ and ϵ of -				
	0	1/4	1/2	3/4	1
1/8	1.412	1.344	1.253	1.134	1
1/4	1.497	1.397	1.278	1.139	1
1/e	1.550	1.430	1.291	1.141	1
1/2	1.598	1.457	1.302	1.143	1

For the particular value of $\Delta W/\eta = 30,000$ Btu per pound, the peak G values associated with entry at limiting speed are indicated in figure 6. For other values of $\Delta W/\eta$ the peak G value may be found by multiplying the values in figure 6 by

$$\frac{\Delta W/\eta}{30,000}$$

The decrease of peak G with increasing ϵ may be regarded as due to the increase in the effective payload fraction which results from the increase of flank losses with ϵ . The effective payload fraction at any instant is the value of μ of a zero-flank-loss vehicle which has the same instantaneous dimensions and the same payload as the actual finite-flank-loss vehicle. It was shown in reference 1 that lower limiting velocities and a broader, lower G pulse result from larger payload inertia.

Representative G pulses associated with the peak values of figure 6 are shown in figure 7. The broadening effects of the larger effective payload inertia are evident in each case for increasing θ_c and ϵ .

The location of the point of peak G is indicated in figure 8. The indicated peak G positions are for a particular choice of values of w , L , and h_s' . For other values, the positions in figure 8 should be shifted by the amount

$$\log_e \left(\frac{L}{8} \frac{w}{140} \frac{25,200}{h_s'} \right)$$

where L is in feet, w is in pounds per cubic foot, and h_s' is in feet. A positive shift is toward zero ω (larger densities) in figure 8. The value of $\omega = \log_e \rho$ corresponding to sea level is nearly -6 with the mass density expressed in English units. Figure 8 may be used in combination with the pulse shapes of figure 7 to establish a largest vehicle which can survive entry. A vehicle of largest size is defined as that which has essentially completed its deceleration at sea level. Sample calculations of this kind are given in references 1 and 4 for vehicles with no flank losses ($\epsilon = 0$).

The trends observed in figure 8 are more complex than those of the peak G values and pulse shapes (figs. 6 and 7). Although the variations are somewhat complicated, the spread in position through the entire θ_c range does not exceed 1.1 generalized scale heights h_s' (one unit of ω equals one scale height h_s') for any ϵ at any value of μ . Through the θ_c range a reversal of trends occurs. At the lower values of θ_c , increasing values of ϵ (higher flank losses) have an effect that resembles an increase of inertia for the case of no flank loss. This is the inertia effect observed for the peak G values and the pulse shapes (figs. 6 and 7). The peak G values thus occur at higher densities. For the steepest flanks, and the associated highest flank losses, the consumption

of material on the flanks is quite significant and begins at higher altitudes. The vehicle tends to be consumed earlier and thus the peak G occurs at lower densities.

In references 1 and 4 deceleration decay lengths in ω were assigned to be measured from the peak G point for each shape. Values of decay length sufficiently large to hold through the limited parameter range of references 1 and 4 were used. A less arbitrary approach seems required for the wide range of ϵ and θ_c values under consideration in the present paper.

Since the G pulses of figure 7 extend to infinity before vanishing, the end of the high-mass-loss region may be conveniently defined in terms of the point at which the G value has dropped to a specified fraction of the peak value. The size which puts this point at sea level may then be defined as the bounding size.

The value of bounding size is quite sensitive to the location of the point chosen to define the end of the G pulse. Consider, for example, the effect of a shift of one-half of a scale height in the altitude of the point at which a specified fraction of peak G is attained. Such a shift means a change of L to $1.65L$ and a change of L^3 (or weight) to $4.48L^3$. Furthermore, a definition based on the decay of the G pulse may become inadequate when velocities are considered. The limiting velocity varies as $\sqrt{\Delta W/\eta}$ so that a change to $\frac{1}{2}\eta$ means a 41.4 percent higher velocity at sea level with no change in the bounding size.

In figure 9 are indicated the altitudes at which the deceleration has fallen to one-thousandth of the peak value. As indicated previously the choice of one-thousandth peak G is somewhat arbitrary. The deceleration at one-thousandth peak G is $\sim 1g$ for $\Delta W/\eta = 30,000$ Btu per pound. The corresponding velocities are $\sim 10^2$ feet per second.

In the tail of the G pulse the ballistic parameter has nearly the same value as at infinity, that is

$$\delta \approx \delta_{\omega+} = \frac{wL}{6} \frac{\mu}{1-\mu} \frac{1}{(1-\epsilon \sin^2 \theta_c)^2} = \frac{a_g h_s'}{2f_{\omega+}}$$

where $f_{\omega+}$ is $f(\lambda_{\omega+})$, so that the values of ω for values of G other than one-thousandth of the peak value may be found approximately from those of figure 9 by inversion of the relation

$$\Delta \log_e G = \Delta \omega - f_{\omega+} e^{\omega} (e^{\Delta \omega} - 1)$$

The ω shifts of the curves in figure 9 with L , w , and h_s' are given by the same expression

of β , where β is related to F_R , as seen in figure 7. The temperature is seen to vary over the range of 108°C to 132°C . This variation is attributed entirely to the variation of the earth-reflected component of radiation since the direct solar and direct earth components are constant during sunlight conditions.

The coldest spot on the balloon will occur in an area where heat input is smallest and will be in an area of the surface that can neither "see" the earth nor the sun. The heat transfer to and from this coldspot is assumed to be entirely radiative since the material is so thin that conduction can be neglected. The heat radiated away from the coldspot surface can be written as

$$\text{Heat out} = (\epsilon_i + \epsilon_o)\sigma T_{C,su}^4 \quad (13)$$

since the shell is so thin that no appreciable temperature gradient can exist between the inside and outside surface. The heat input will come entirely from the inside of the satellite (because the outside surface is "looking" at the cold environment of space) and can be written as

$$\text{Heat in} = \epsilon_i \sigma \bar{T}_{su}^4 \quad (14)$$

which is the quantity of heat received by all surface elements inside the spherical shell because of the internal radiative heat transfer (ref. 2). By setting equation (13) equal to equation (14), the coldspot temperature can be calculated with respect to the average temperature to give

$$T_{C,su} = \left(\frac{1}{1 + \frac{\epsilon_o}{\epsilon_i}} \right)^{1/4} \bar{T}_{su} \quad (15)$$

The hottest spot on the satellite will occur at a point where the sun's rays are normal to the surface since at this point the heat input is greatest. If only radiative heat transfer to and from this element of shell is considered, the heat output can be expressed as

$$\text{Heat out} = (\epsilon_i + \epsilon_o)\sigma T_{H,su}^4 \quad (16)$$

The heat input at equilibrium can be expressed as

$$\text{Heat in} = \epsilon_i \sigma \bar{T}_{su}^4 + \alpha_s C_s \quad (17)$$

where the first term describes the heat input to the inside surface and $\alpha_s C_s$ describes the input on the outside from direct solar radiation. By setting equation (16) equal to equation (17), the hotspot temperature can be calculated with respect to the average temperature as

$$T_{H,su} = \sqrt[4]{\left(\frac{\alpha_s}{\epsilon_i + \epsilon_o}\right) \frac{C_s}{\sigma} + \left(\frac{1}{1 + \frac{\epsilon_o}{\epsilon_i}}\right) \bar{T}_{su}^4} \quad (18)$$

The hotspot and coldspot temperatures corresponding to the average satellite temperature \bar{T} while in the sunlight are shown in figure 9 for Echo I where $\epsilon_o = 0.03$, $\epsilon_i = 0.45$, and $\alpha_s = 0.10$. It is important to know the coldspot temperature since this temperature must be considered as the operating temperature when determining vapor pressure produced by a subliming compound used for inflation. (The coldspot can be as large as one-eighth the total satellite surface.) The hotspot is required in evaluating adhesives for sealing the satellite gores together under conditions of maximum temperature and internal-pressure-developed skin loading as well as other structural considerations. It can be seen from equation (12) that the variable parameter affording major control of the average satellite temperature \bar{T} is α_s/ϵ_o while the temperature variation over the surface of the satellite can be minimized by making ϵ_o/ϵ_i as small as possible, as can be seen from equations (15) and (18). The relations among these three temperatures over a wide range of altitudes can be seen in figure 10. For example, at 927 kilometers the average

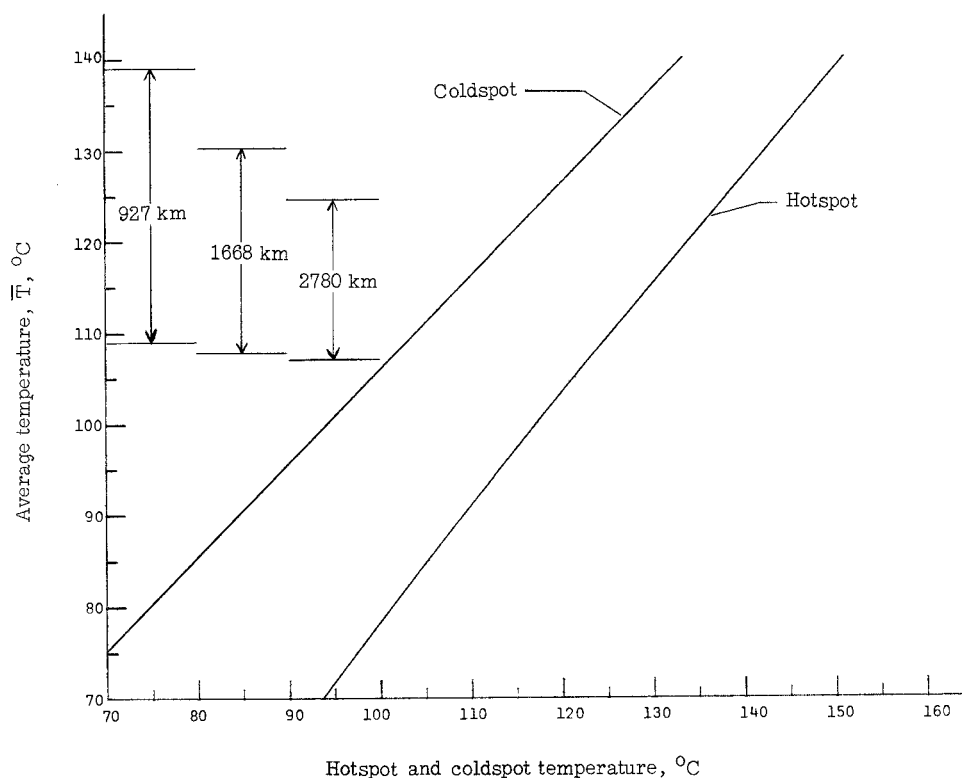


Figure 10.- Predicted variation of the Echo I hotspot and coldspot temperature with satellite average temperature. Average satellite temperatures possible while in the sunlight at three circular orbit altitudes are included.

temperature in the sunlight varies over the range 109°C to 139°C while the coldspot varies from 103°C to 132°C and the hotspot from 125°C to 150°C . It will be noticed that the minimum coldspot temperature on the satellite while in sunlight is affected only slightly with rather wide ranges of altitude, while the maximum hotspot is affected to a greater extent.

The equilibrium temperature of the satellite while in the shadow of the earth is determined by making the appropriate substitutions into equation (7), where the first two terms are now zero. The resulting equation is

$$\bar{T}_{\text{sh}} = \sqrt[4]{\frac{C_S \alpha_E}{4\epsilon_0 \sigma} \frac{1-a}{2} \left[1 - (1-k^2)^{1/2} \right]} \quad (19)$$

A solution of this equation shows that the equilibrium temperature of a spherical satellite in the earth's shadow at an altitude of 1668 kilometers is -107°C . It is noted from this equation that the average equilibrium temperature in the shadow is independent of the thermal radiation characteristics of the satellite's surface when α_E is assumed equal to ϵ_0 . This assumption can be made as a first approximation since the thermal radiation wavelength of both the earth and the satellite are of the same order of magnitude.

Thermal response.— The equilibrium temperature analysis presented above is indicative of the satellite temperature only if the satellite remains in the particular environment for a period of time sufficient for thermal equilibrium to be established. To predict the satellite temperature over a complete orbit, it is necessary to calculate the dynamic thermal response as it passes from one environment to the next. In the sunlight, the thermal environment changes as a result of variations in the earth-reflected radiation input. As the shadow is entered, the environment changes abruptly as the solar radiation is completely cut off. Equations for determining the dynamic thermal response of the satellite as it enters and exits the earth's shadow are derived in appendix A. The first case considered is that of entering the earth's shadow and is expressed as

$$t_{\text{sh}} = \frac{y^2}{2wx\sqrt{\frac{w}{x}}} \left(\tan^{-1} \frac{\bar{T}}{\sqrt{\frac{w}{x}}} - \frac{1}{2} \log_e \frac{\bar{T} - \sqrt{\frac{w}{x}}}{\bar{T} + \sqrt{\frac{w}{x}}} \right) \Bigg|_{\bar{T}_0}^{\bar{T}} - \frac{z^2}{4wx} \left(\log_e \frac{\bar{T}^2 - \frac{w}{x}}{\bar{T}^2 + \frac{w}{x}} \right) \Bigg|_{\bar{T}_0}^{\bar{T}} \quad (20)$$

The temperature decrease as a function of time predicted by this equation is seen in figure 11 where the specific heat of film was taken as $-1.14 \times 10^{-2} + 9.35 \times 10^{-4}\bar{T}$. The average satellite temperature was assumed to be 108°C as the shadow was entered. (See fig. 9.) A study of equation (20) shows that the rate at which the satellite cools is not independent of the surface characteristics as was the case for thermal equilibrium in the shadow. The higher, the emittance, the faster it will cool. Echo I, however, has a very low outside emittance (0.03), yet rapid cooling is evident. This property, of course, is due to its very low ratio of mass to area.

The second case considered is that of leaving the low-temperature environment of the earth's shadow and entering the sunlight. The equation for expressing the thermal response for this case is

$$t_{su} = \frac{y^2}{2w_1x\sqrt{\frac{w_1}{x}}} \left(\tan^{-1} \frac{\bar{T}}{\sqrt{\frac{w_1}{x}}} + \frac{1}{2} \log_e \frac{\sqrt{\frac{w_1}{x}} + \bar{T}}{\sqrt{\frac{w_1}{x}} - \bar{T}} \right) \Bigg|_{\bar{T}_0}^{\bar{T}} + \frac{z^2}{4w_1x} \left(\log_e \frac{\frac{w_1}{x} + \bar{T}^2}{\frac{w_1}{x} - \bar{T}^2} \right) \Bigg|_{\bar{T}_0}^{\bar{T}} \quad (21)$$

The temperature increase as a function of time predicted by this equation is also plotted in figure 11. It will be noticed that the initial temperature for

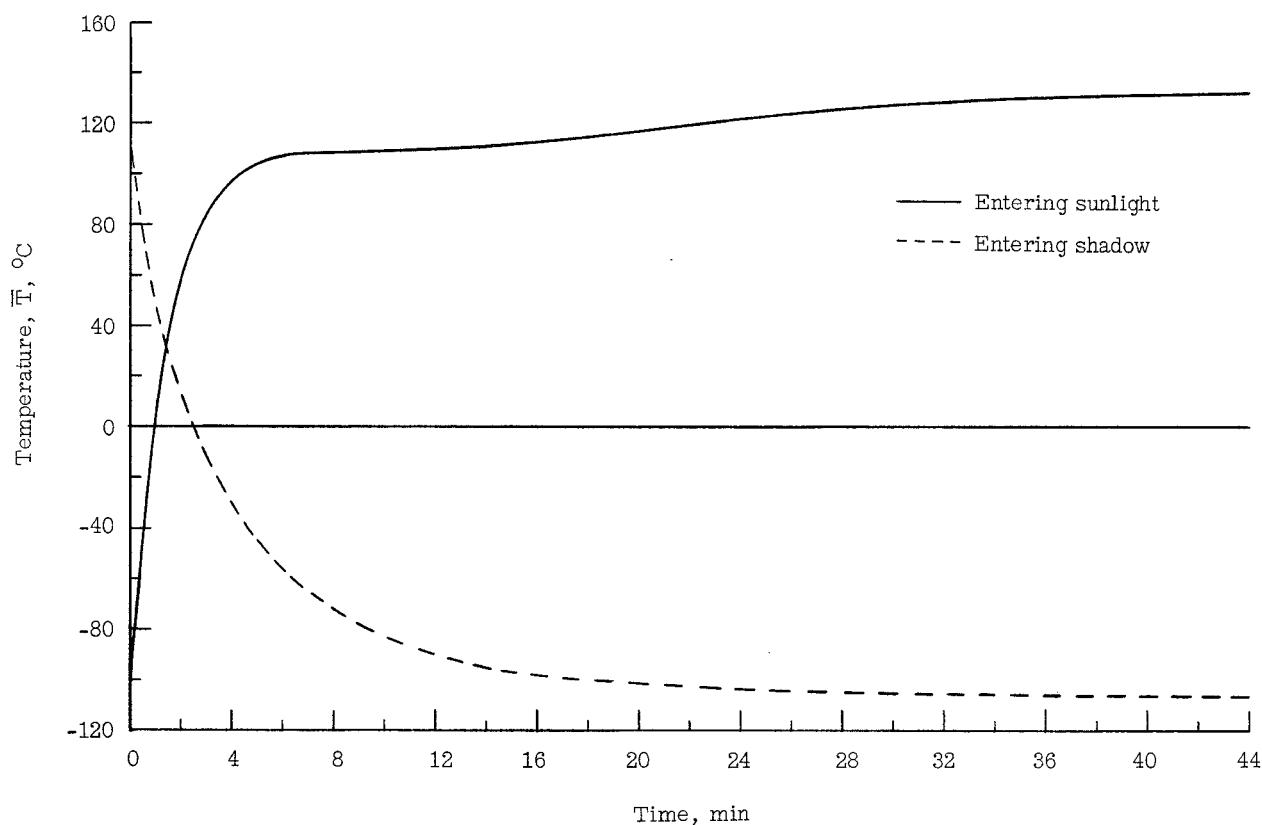


Figure 11.- Predicted thermal response of Echo I as it enters and leaves the earth's shadow.

this curve was taken as the equilibrium or minimum temperature that could be attained in the shadow, the reason being to show the maximum time required for the satellite to reach thermal equilibrium after entering the sunlight. The curve shows a very rapid increase in temperature, that is, from -107°C to 102°C in approximately 6 minutes.

In a circular orbit at an altitude of 1668 kilometers, the satellite travels at a rate of approximately 15° in 5 minutes. It is seen (fig. 9) that the reflected earth radiation does not begin to change the satellite temperature until an angular distance β of about 30° from the shadow has been reached. Therefore, it can be concluded that the satellite has reached thermal equilibrium with its environment after leaving the earth's shadow before the reflected earth radiation becomes appreciable. Because of this rapid thermal response of the satellite, it has been assumed that once the satellite has reached 108°C after leaving the earth's shadow, it remains in thermal equilibrium with its sunlight environment. Hence, temperature increases in figure 11, shown subsequent to 5 minutes after leaving the shadow, are due to increased thermal energy input from the earth-reflected component as the satellite moves toward the sun while in an orbit where δ is 90° .

In calculating these thermal-response characteristics of Echo I, the thermal mass of the inflation powders was not included. The predicted thermal response curves may be considered a bit severe for the initial life of the satellite, but they become more representative of the actual conditions toward the end of the test period when most of the powder has leaked out.

The temperature variations of the satellite have thus far been calculated for sunlight portions of its orbit (fig. 9) as well as for transitions in and out of the shadow (fig. 11). Temperature predictions will next be made for complete orbits. The particular orbits for which these calculations are made can be described by use of the circular orbit geometry seen in figure 5. Calculations were made for arbitrarily selected values of δ of 90° , 60° , 40° , and $\leq 37.25^\circ$ as seen in figure 12. When δ equals 90° , the most severe thermal

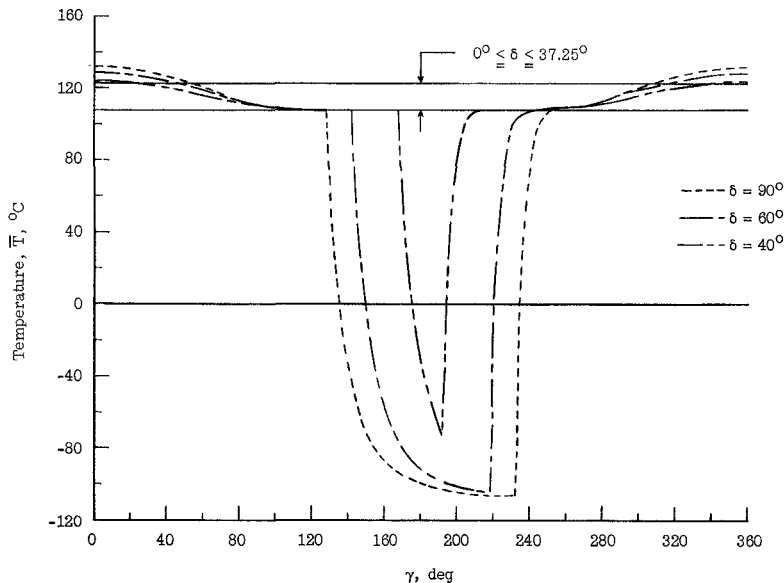


Figure 12.- Predicted variation of Echo I temperature as it traverses orbits where the normal to the orbital plane is inclined at various degrees to the earth-sun line.

excursions will be experienced because the maximum period of time will be spent in the shadow. The satellite will also pass directly between the earth and sun during this orbit and will attain the maximum temperature. The temperature decrease from 132°C to 108°C , seen to occur in the interval $0^{\circ} \leq \gamma \leq 128^{\circ}$, results from the decrease in earth-reflected radiation. When entering the shadow, the temperature decreases from 108°C to -107°C ; whereas when leaving the shadow, the temperature increases rapidly to 108°C with more gradual increase in temperatures above 108°C and reaches 132°C again as it passes between the earth and sun. The variation of temperature around this orbit is from 132°C to -107°C or a change of 239°C . The temperature variations while traversing the orbits of δ equal to 60° and 40° are seen to be over a range of 234°C and 197°C , respectively. For all angles of $\delta \leq 37.25$ which are continuous sunlight orbits, however, the variation is maintained within the range 108°C to 122°C as indicated by the solid lines in figure 12. As δ decreases from 37.25° , the variations in temperature over a complete orbit will decrease and will become constant at about 110°C when δ is 0° .

These analyses have shown that the satellite will experience very large temperature variations when it passes through even the slightest portion of the earth's shadow as a result of its small thermal mass-to-surface area ratio. Continuous sunlight orbits, on the other hand, can be established with a rather wide degree of flexibility in that the normal to the orbital plane can precess within a solid angle of $2\delta = 76^{\circ}$ about the earth-sun line for a 1668-kilometer circular orbit, while the satellite will always remain in sunlight and experience average temperature variations in the interval 108°C to 122°C . The hot-spot and coldspot temperatures for these conditions will vary in the interval 124°C to 137°C and 102°C to 117°C , respectively. For these reasons, the Echo I satellite was launched into an orbit such that the satellite would remain in continuous sunlight for the first two weeks; thus the temperature-sensitive pressure-producing subliming compounds would remain effective for the duration of the test period.

Micrometeoroid Impact and Penetration

The Echo I satellite being constructed of such a very thin plastic film is expected to be highly vulnerable to micrometeoroid puncture. All particles with sufficient energy will penetrate through the film and will make small holes through which the inflation gases and vapors can leak out.

Until recently, meteor studies have been limited to photographic and radar echo techniques effective in detecting particles with a mass of about 10^{-4} grams (ref. 4) or greater. With these techniques, the number and velocity can be measured directly while the mass and size can be inferred by some theoretical considerations. In the past few years, rocket and satellite vehicles have afforded the opportunity to perform micrometeoroid impact experiments outside the earth's atmosphere.

The problem as to size and influx of meteoritic particles has been treated in reference 5 with the reservation in mind that the basis for extrapolating the distribution function is not supported by direct evidence. The influx

distribution was determined by beginning with the Millman point (that is, the total number of particles incident on the earth per square meter per second determined by Millman's visual observation) and taking the naked-eye threshold as fifth visual magnitude. The influx of particles is assumed to increase by a factor of $10^{0.4}$ (or 2.512) per magnitude step. The mass distribution was determined by taking the mass of a zero magnitude particle as 25 grams on the basis of the Harvard photographic meteor study (ref. 5) while assuming the mass decreases by a factor of $10^{0.4}$ per magnitude step. This distribution is shown in figure 13 as the theoretical extrapolation.

Direct evidence from micro-meteoroid experiments as to the influx of particles with masses of the order of 10^{-9} grams or greater indicates that the influx distribution increases by a slightly higher factor of $10^{0.435}$ (or 2.720) while the mass distribution factor is assumed to remain the same. This new factor is calculated from the experimental extrapolation curve seen in figure 13. It is interesting to note the nearness of this experimentally inferred value of 2.720 to that of the ever-occurring mathematical constant e (that is, $e = 2.718$).

This curve was constructed by taking the Millman point and the 1959 Eta [Vanguard III] (ref. 6) data points as the most reliable points presently available; the Millman point was chosen because it comes from naked-eye observations and the 1959 Eta point, because it has collected more data from a statistical point of view than any other satellite. Two other experimental points have been plotted in figure 13, 1958 Delta [Sputnik III] (ref. 7) and 1958 Alpha [Explorer I] (ref. 8), the first agreeing somewhat with the theoretical extrapolation and the latter agreeing very well with the Millman - 1959 Eta extrapolation. This agreement further increases the evidence of a higher influx rate than that assumed in the theoretical extrapolation. The satellite data used here were taken from vehicles orbiting at altitudes in the vicinity of the Echo I vehicle. Their apogee-perigee altitudes varied in the interval 300 to 2500 kilometers compared with a circular orbit altitude of about 1668 kilometers for Echo I. This variation is mentioned in light of the possibility that there may be some appreciable variation of influx with altitudes, possibly in orders of magnitude, although there is no evidence to support such a contingency.

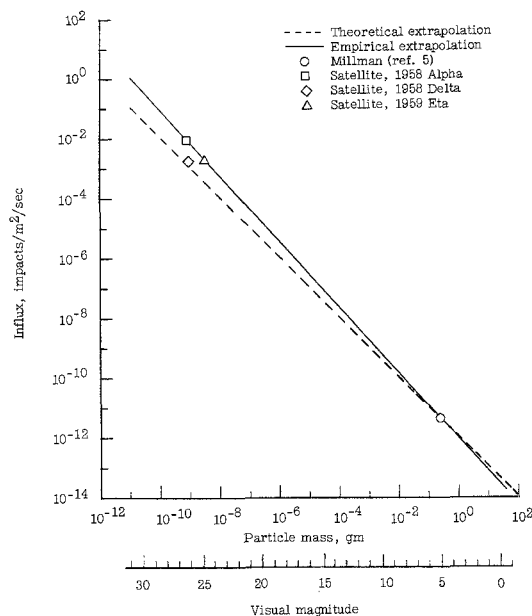


Figure 13.- Comparison of theoretical values with satellite data for micrometeoroid mass and influx distribution.

An approach to the problem of estimating the rate of hole growth due to micrometeoroids striking the satellite can probably be most easily explained by use of table I (patterned after Whipple's table in ref. 5). The columns have the following meaning:

① - Visual magnitude of meteor is shown.

② - Mass, grams: The mass is assumed to decrease by a factor of $10^{0.4}$ for each visual magnitude increase step. This relation can be expressed mathematically as

$$m_u = \frac{25}{10^{0.4u}} \quad (22)$$

for each visual magnitude in question.

③ - Radius, centimeters: The radius of a particle of given mass is calculated by assuming a spherical shape and constant density. The density is assumed to be 2.06 gm/cm^3 . This density was calculated from a number of considerations. The recovered meteorites that have been analyzed show a composition of iron and stone. It has been reported (ref. 9) that there are from 4 to 9 times as many stones as irons. If an average composition of 6.5 stones to 1 iron is assumed, an average density of 4.07 gm/cm^3 is calculated. It is reported (ref. 5) that evidence is extremely strong, although not conclusive, that the density of ordinary meteoroids is 0.05 gm/cm^3 . If these values are assumed as upper and lower density extremes, the average approximation is taken as 2.06 gm/cm^3 . Therefore, the radius of a particle of any visual magnitude can be expressed as

$$R_u = \left(\frac{2.8987}{10^{0.4u}} \right)^{1/3} \quad (23)$$

④ - Particle cross-sectional area, square centimeters: This number is the cross-sectional area of each particle size calculated from the radii given in column ③ and is seen to be

$$A_u = \left(\frac{16.1284}{10^{0.4u}} \right)^{2/3} \quad (24)$$

⑤ - Influx of micrometeoroids on the earth's surface per square meter per second: This number includes all particles of mass equal to or greater than that appearing in the line in question. For any visual magnitude, this number can be expressed as

$$I_u = 3.0480 \times 10^{-14} \times 10^{0.43457u} \quad (25)$$

This number is derived from Millman's observation of 2×10^8 naked-eye meteors striking the earth per day where the threshold of the human eye is taken to be fifth visual magnitude.

⑥ - Influx of micrometeoroids on Echo I per second: This number includes all particles of mass equal to or greater than that appearing in the line in question. The number is determined by multiplying one-half the surface area by equation (25). The factor $1/2$ is a correction factor necessary to account for the shielding of the satellite by the earth and is valid at altitudes up to about 10^4 kilometers. (See ref. 5.) This number can be expressed as

$$I_u = 4.446 \times 10^{-11} \times 10^{0.4346u} \quad (26)$$

⑦ - Influx of micrometeoroids on Echo I for any visual magnitude per second: This number includes all particles within one visual magnitude interval centered around the mass of the particle in the line in question. For example, the line of visual magnitude 10, column ⑤, gives a number of 6.757×10^{-10} which is a cumulated number of particles and indicates all those with masses of 2.5×10^{-3} grams or greater. The average number of particles of average mass 2.5×10^{-3} grams is determined by assuming one-half the particles between visual magnitude 9 and 10 as well as one-half the particles between visual magnitude 10 and 11 to have this mass. This number can be expressed as

$$I_u = 4.446 \times 10^{-11} \left[\frac{10^{0.4346(u+1)} - 10^{0.4346(u-1)}}{2} \right] \quad (27)$$

⑧ - Rate of hole growth in Echo I, square centimeters per second: This number is the rate at which penetration by micrometeoroids with masses of those in the line in question produces holes in the satellite wall through which it passes. The number is calculated by multiplying the cross-sectional area taken from the line in question in column ④ by the average number of particles with the same size taken from column ⑦.

The total rate of hole growth in the satellite is found by adding the contribution of each size particle with energies sufficient to penetrate through the satellite skin in the visual magnitude interval 0 to 31. Zero will be taken as the upper limit because the probability of a larger particle striking the satellite is negligible, and 31 as the lower limit because the solar radiation pressure will not permit those with smaller energies to exist in the vicinity of the earth. (See ref. 5.) The depth of penetration can be calculated by use of the equation (from ref. 5)

$$d = \left(\frac{9}{\pi \rho' \xi} \right)^{1/3} (E_k)^{1/3} \quad (28)$$

where the kinetic energy E_k of the particles is based on a velocity of 15 kilometers/sec for those in the visual magnitude interval 20 to 31. If the density of the film ρ' is taken as 1.38 gm/cm^3 and the heat to vaporization ζ as $4.98 \times 10^9 \text{ ergs/gm}$, equation (28) gives a penetration depth of 1.68×10^{-3} centimeters for particles of visual magnitude 31. This result means that all particles are capable of penetrating the 1.27×10^{-3} -centimeter-thick poly[ethylene terephthalate] film. No micrometeoroid buffer action by the 2,200 angstroms of vapor-deposited aluminum is assumed. By adding the rate of hole area contributions for each visual magnitude in column (8), for lines 0 to 31, it is found that holes will be made in the satellite at the rate of 1.63×10^{-4} square centimeters per second. The penetration depth, given by equation (7), is based on a hole shaped in the form of a right circular cone with total apex angle of 60° . If this shape is assumed to be a fairly accurate approximation of the hole shape actually produced, then it is easily seen that the particles with energies barely sufficient to penetrate but not pass through will not result in holes as large as their cross-sectional area. On the other hand, speculations have been made in this field that indicate a hole larger than the particle cross-sectional area will be produced by particles with sufficient energy to pass through the satellite wall and, in addition, that some of the more energetic ones may pass through the wall twice. These questions and others have led to studies of high-velocity-particle impact phenomena. Thus far, micrometeoroid velocities have not been obtained in laboratories. In view of the questions presently unanswered, an arbitrary correction factor of 2 is assigned to the calculated hole-growth rate; this factor gives 3.25×10^{-4} square centimeters per second which hereafter is taken as the hole-growth rate due to micrometeoroid bombardment in the Echo I satellite.

Deforming Loads

While experimentally evaluating the Echo I satellite as a passive radio relay station, it is necessary that its shape be well defined. The isotropic characteristic of the sphere eliminates any requirement for axial orientation. After the satellite is erected to its spherical configuration, there are four known sources capable of producing deforming loads of sufficient magnitude to warrant consideration: (1) The atmospheric molecules will develop a static pressure as well as a dynamic pressure, (2) impinging micrometeoroids will produce a pressure, (3) the sun will develop a solar radiation pressure, and (4) the memory that the satellite retains of its folded condition can cause preferential deformation of the surface along fold lines.

Static atmospheric pressure.- The static pressure of the atmosphere up to an altitude of 700 kilometers is taken from reference 10. An extrapolation has been made in the interval 700 to 2000 kilometers. The results can be seen in figure 14.

Dynamic atmospheric pressure.- The dynamic pressure under consideration is that pressure developed at the stagnation point. It is assumed that the mechanical interaction between the atmospheric molecules and the satellite is purely elastic. This assumption simplifies the analysis and results in a conservative estimate in light of the objective, which is to show eventually that

the inflation and pressure sustenance system will be expected to keep the satellite in a spherical shape for the 1- to 2-week test period. Free molecular flow will exist at the altitudes of interest where the mean free path is of the order of hundreds of kilometers. Under these conditions the number of molecules striking the satellite per unit surface area at the stagnation point will be

$$nv_B t \quad (29)$$

The momentum transfer of each of these molecules will be $2mv_B$, if the satellite velocity is assumed to be much greater than the thermal velocity of the molecules. The time rate of change of the momentum will be

$$\frac{(nv_B t)(2mv_B)}{t} \quad (30)$$

This relation is recognized as the impulsive force from which the pressure or force per unit area can be written as

$$p = 2\rho v_B^2 \quad (31)$$

where ρ is the atmospheric density. The satellite velocity for a circular orbit is

$$v_B = \sqrt{\frac{g_0 R_E^2}{R_E + h}} \quad (32)$$

The densities up to an altitude of 700 kilometers were taken from reference 4 and extrapolated from 700 to 2000 kilometers. By substituting these densities and the velocities from equation (32) into equation (31), the dynamic pressure was calculated and can be seen in figure 14. It will be noticed from this figure that the static pressure is about one-hundredth that of the dynamic pressure above 600 kilometers. In a 1668-kilometer circular orbit, the dynamic pressure at the stagnation point is found to be 5.624×10^{-10} torr.

Micrometeoroid pressure.— The pressure resulting from the impingement of micrometeoroids on the surface of a satellite can be estimated on the basis of the number and size distribution of cosmic dust particles believed to exist in the earth's vicinity of space. It will be assumed that the impacting micrometeoroids are distributed uniformly over a plane surface normal to the direction of motion, have a uniform spatial distribution, and that the particles are stopped completely by the surface. The satellite velocity is neglected in

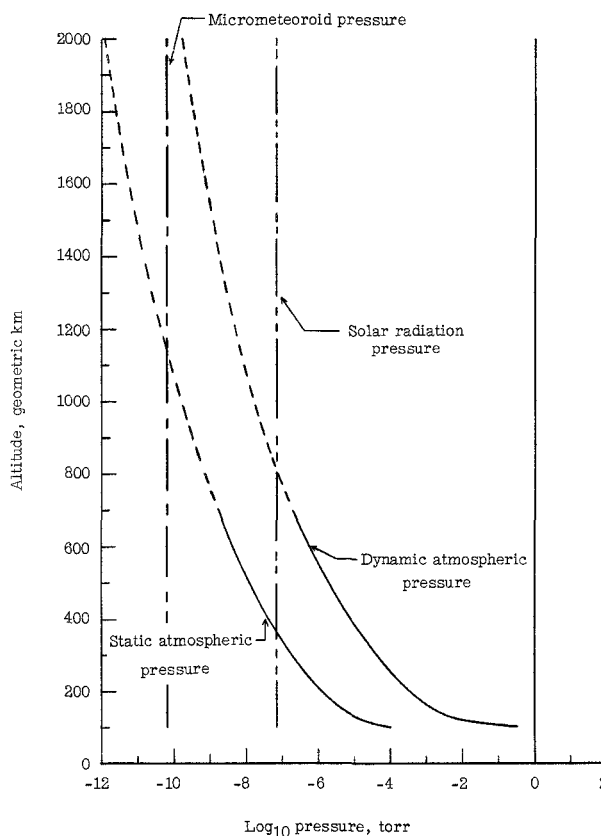


Figure 14.— Comparison of four sources of external pressure above 100 kilometers altitude.

computing the momentum change of the particles since it is only about one-third the micrometeoroid velocities of 15 to 28 kilometers per second given in reference 5. Based on these assumptions, the pressure resulting from this source can be computed from the time rate of change of the particles' momentum per unit of surface area which is

$$p = \sum_{u=0}^{u=31} n_u m_u v_u \quad (33)$$

The magnitude of n_u can be determined by dividing column (7) in table I by half the Echo I surface area, m_u can be taken directly from column (2) in table I, and v_u is obtained from reference 5. The pressure computed from equation (33) is 6.48×10^{-11} torr which is considered a maximum value applicable to Echo I from this source because the particles all have sufficient energy to pass through the thin film used for fabrication; hence all their momentum will not be given up at the surface. This pressure is seen (fig. 14) to be independent of altitude and about one order of magnitude less than the dynamic atmospheric pressure at Echo I altitude.

Solar radiation pressure.- The solar radiation pressure is proportional to the normally incident energy flux C_s taken as 1.395×10^6 ergs/cm²-sec at 1 astronomical unit from the sun. An equation for expressing the pressure produced by this radiation is given in reference 11 as

$$p_n = \frac{2C_s}{c} \quad (34)$$

In the derivation of this equation, it was assumed that the solar energy was incident normal to the surface of a perfectly specular reflecting mirror. The surface of the satellite approaches these conditions. There will always be a point on the surface where the radiation is at normal incidence due to the satellite's spherical symmetry, and although the vapor-deposited aluminum surface absorbs about 10 percent of the incident solar radiation, the pressure predicted by equation (27) can be considered as an upper limit as a result of this source. From equation (34) it is found that the solar radiation pressure is 6.91×10^{-8} torr or 123 times as great as the dynamic atmospheric pressure at an altitude of 1668 kilometers. This pressure is plotted as a constant in figure 14 for further comparison of the deforming pressures present in the environment of space. It is interesting to note that the solar radiation pressure is greater than the dynamic atmospheric pressure above about 800 kilometers and greater than the static atmospheric pressure above about 360 kilometers.

Memory of folds.- As the satellite is compactly folded and packaged into its 67.31-centimeter container, folding angles of 180° are made. The folds are all subjected to a 1-atmosphere loading during the packaging process by placing the folded balloon inside a plastic bag and evacuating the bag so that the external atmospheric pressure will compress it to a minimum size. This process yields the plastic film along the fold lines so that when the load is removed it is left permanently set. When the satellite is inflated, it will retain a memory of these folds unless the material is again yielded after the satellite

becomes spherical. It would require about 58.96 kilograms of benzoic acid to produce an internal pressure large enough to stress the film skin to its 8.96×10^8 dyne/cm² (ref. 12) yield point. Since this weight far exceeds the payload weight limitations, the alternate solution of maintaining a positive internal pressure was employed.

The critical buckling pressure of a smooth thin-wall sphere can be determined theoretically from the equation

$$P_{cr} = \frac{2Et'^2}{R^2\sqrt{3(1-\nu^2)}} \quad (35)$$

taken from reference 13. If it is assumed that Echo I is such a smooth sphere, this pressure is found to be 2.28×10^{-5} torr, where the modulus of elasticity of the film was taken as 3.80×10^{10} dynes/cm² (ref. 12) and Poisson's ratio was assumed to be zero.

From this analysis of deforming loads, it can be seen that the critical buckling pressure of the Echo I satellite based on equation (35) is much greater than the deforming pressures present in the environment of space. However, the memory effect of this satellite makes it imperative that a small skin stress be maintained to prevent the surface from collapsing. If it were possible to remove the memory, the satellite would not require a sustained pressure to maintain sphericity nor would it be expected to buckle (on the basis of eq. (35)) until it had come down to an altitude of about 250 kilometers.

INFLATION MEDIUM

Considerations

In the design of an inflation system for large, inflatable satellites, the prime considerations are that it be simple, lightweight, and reliable. The inflation system must be initiated after the satellite has been transported through the dense atmosphere of the earth inside a closed container and released in orbit into the vacuum of space. Past conventional methods of inflation have utilized compressed gas where the bottles and ejection system consume most of the inflation-system weight; the bottles, however, are susceptible to leakage and are difficult to store. A system based on the sublimation principle is investigated herein and is predicted to be quite satisfactory. In this application no bottles are used and the inflation compound is distributed inside the sphere in a loose powder form in such a manner that it lends itself very well to folding and packaging techniques.

Careful consideration must be given to the amount of residual air that can be tolerated inside the packaging container yet outside the balloon, as well as the amount of air left inside the balloon. If the container were closed with 1 atmosphere absolute pressure inside, the balloon would virtually explode when released in the vacuum of space. Appreciable moisture or other volatile condensables inside the balloon would also result in rather explosive inflation. To prevent either of these occurrences, the container for the Echo I satellite

was designed to maintain a vacuum. It was determined experimentally that a pressure of 1 to 3 torr could be tolerated inside the container without resulting in too rapid inflation as well as being low enough for the moisture content to evaporate and be pumped away during the evacuation process of the canister. This pressure is sufficiently high to prevent the low vapor pressure inflation compounds from subliming out of the folded balloon through the small holes placed in it to allow the water vapor and residual air to be pumped away during the evacuation. There were 244 holes, hereafter referred to as air orifices, placed in the sphere, 1.59 millimeters diameter, and located along the outside of each fold to allow air flow with a minimum amount of restrictions during the evacuation. These holes had a total area of 4.84 square centimeters.

When it is necessary, as in the case for Echo I, to maintain a pressure inside the satellite after inflation, the inflation system weight can be utilized more efficiently by using two subliming compounds. One of the compounds was used for generating a sufficiently high vapor pressure to break the unfolding loads and erect the balloon to its full size, and a second compound with a lower vapor pressure, under the same temperature conditions, to maintain inflation for the desired period of time. The lower vapor pressure compound will not be lost as fast through the air orifice and micrometeoroid holes in the skin as the more volatile, initial inflation compound; thus, less weight is required.

The vapor pressure of a subliming compound in solid-vapor equilibrium varies according to the integrated Clausius-Clapeyron equation which is

$$p = c' \exp\left(-\frac{\lambda}{R_g T}\right) \quad (36)$$

It will be noted from this relation that the equilibrium vapor pressure of the compound increases exponentially as its temperature increases linearly, the assumption being made, of course, that the latent heat of sublimation remains constant over the range of interest. This condition suggests that a subliming compound can be chosen with a low equilibrium vapor pressure at room temperature (20° C) which will have a much higher equilibrium vapor pressure when the satellite is deployed in space and is subsequently heated from the direct solar, earth-reflected solar, and direct earth radiant heat input. As the temperature of the subliming powder inside the satellite rises, its vapor pressure will rise to such a point that the satellite begins to unfold. To compensate for volumetric expansion during inflation, the subliming powder will act as a gas generator to maintain vapor pressure equilibrium.

The rate of inflation from the time the satellite is released in the vacuum of space until it reaches full size will depend primarily upon the residual air left inside the satellite, the sublimation rate of the powder, and the mechanical forces required to unfold and erect the sphere. The rate of inflation resulting from the subliming of the powders is dependent on both the geometric cross section and the effective solar absorptivity of the satellite which are interdependent and do not lend themselves to any known degree of reliable prediction. The time that it takes for inflation, however, can be determined with a fair degree of accuracy by experimental methods.

Radar signals returned from the inflating sphere will display a high degree of scintillation while inflation is occurring. Once the inflation motion ceases, the radar return should exhibit no scintillation after it has been corrected for any periodic low-frequency satellite spin scintillation. These data will give a fair approximation as to the degree of inflation by estimating the geometric cross section from the radar cross section. The accuracy of this method increases with degree of inflation and should be excellent at 100-percent inflation.

Even though the transient inflation is governed by a number of interdependent parameters that do not lend themselves to current theoretical analysis, the fully inflated state can be investigated by a rather straightforward method. The internal pressure required for a thin-wall spherical satellite is determined from the desired stress level in the skin and can be calculated from

$$p_i = \frac{4t'S}{D} + p_o \quad (37)$$

If the internal pressure required and the temperature environment in which the subliming compound must function are known, a compound can be selected that best satisfies these conditions.

There are perhaps four potential sources of pressure generation that are, to a large extent, inherently associated with an inflatable structure of this nature that should be considered. These sources are (1) the expanded atmospheric gases left inside the sphere during packaging, (2) desorbed gases from the fabrication material, (3) thermal radiation within the sphere, and (4) the vapor pressure of the fabrication material.

The expansion of the free atmospheric gas can be computed from the volumetric expansion during inflation by assuming an isothermal transition to give maximum residual pressure. The volume inside the Echo I sphere increases by a factor no less than 1.3×10^5 with a resulting pressure no greater than 2.31×10^{-5} torr based on an initial pressure of 3.0 torr.

Atmospheric gases and vapor (adsorbates) attached to the inside surface of the packaged sphere may be partially or completely desorbed when the satellite is released in space, inflated, and heated. Adsorbates are usually assumed to be attached to the surface of solids by nonspecific forces of attraction between gas and solid such as Van der Waals forces that give rise to physical adsorption and by chemical bonds formed between the gas and solid generally referred to as chemisorption. As a general rule when the adsorbates are below their critical temperature, multilayer adsorption takes place through both physical and chemical bonding whereas at higher temperatures chemisorption only occurs and is usually limited to monolayer thickness. (See ref. 14, ch. IX.) Since water vapor is the only adsorbate present in the atmosphere during satellite preparation that has a critical temperature greater than normal room temperature (that is, 20° C), it will be most susceptible to the more consequential multilayer adsorption. It has been further observed through the study of the isothermal adsorption characteristics of adsorbates that, generally, monomolecular, adsorption prevails at pressures of 0.1 or less than that of saturation, whereas multilayer adsorption prevails at higher pressures and increases with increasing

pressure until saturation is reached. (See ref. 14, p. 519.) For lack of a more quantitative approach to predicting the adsorption and adsorbate characteristics of the solids and adsorbates in question, a prediction is made on the qualitative analysis presented.

The partial pressure of water vapor inside the Echo I canister must be less than the 1 torr to 3 torr absolute pressure permitted which is approximately 0.1 of the 17.5-torr saturation pressure; this requirement places it in the monomolecular adsorption region. The pressure increase resulting from desorption of these adsorbates can be expressed as

$$p = \frac{Nk'T}{V_B} \quad (38)$$

where N is the total number of molecules desorbed. If the monomolecular covering power of water vapor is taken as $5.27 \times 10^{14} \frac{\text{molecules}}{\text{cm}^2 - \text{monolayer}}$ (ref. 15, p. 36), equation (38) can be rewritten as

$$p = \frac{162.796j}{D_B} \quad (j \geq 1) \quad (39)$$

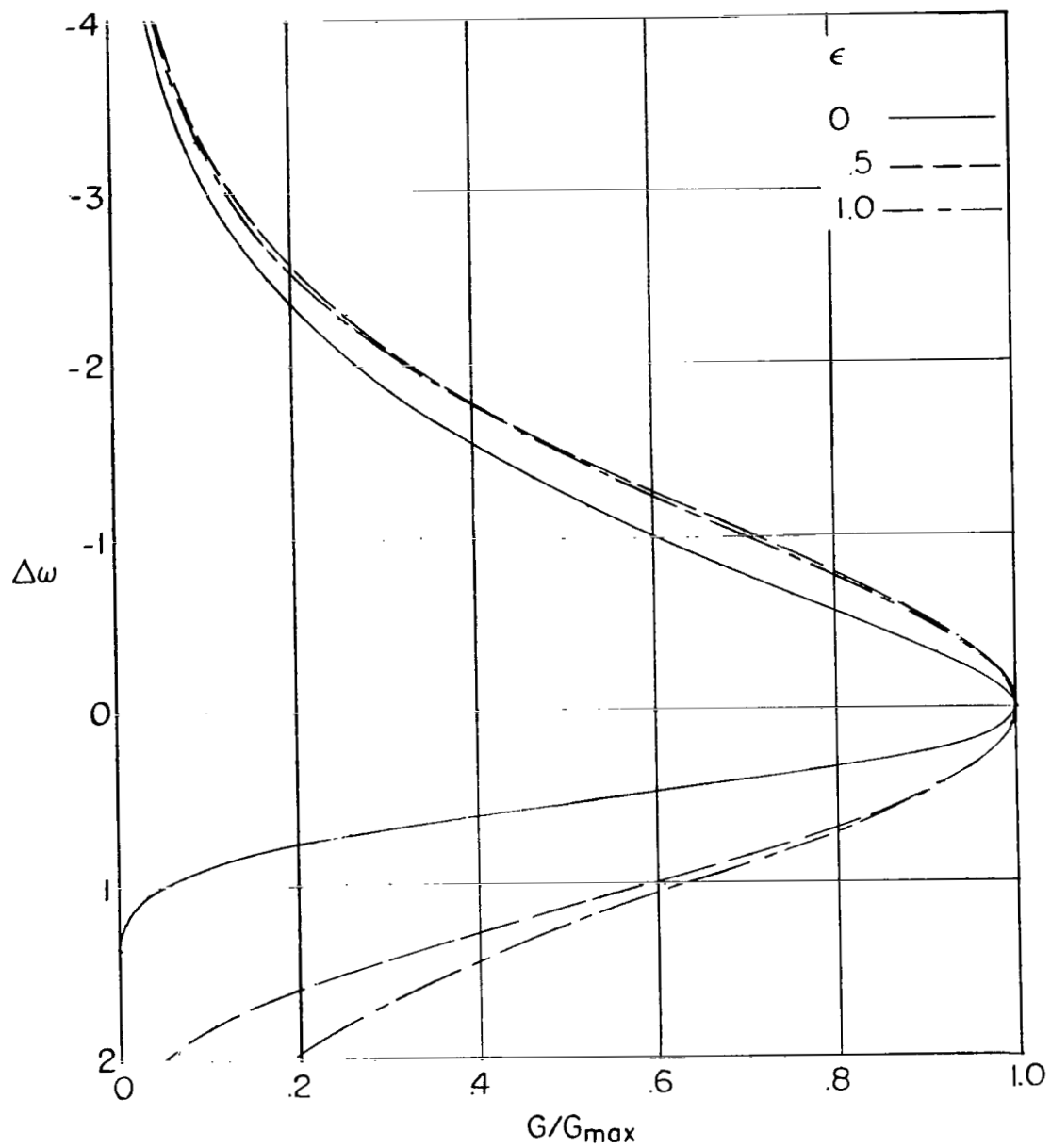
per monolayer of desorbed water where j is the ratio of microscopic surface area to apparent surface area. Since the plastic film is a continuous sheet essentially free of pinholes (ref. 12, p. 2,293) j will be taken as 1.0 and the pressure inside the Echo I sphere produced by a monolayer of desorbed water vapor will be 4.0×10^{-5} torr.

The pressure produced inside a thin-wall spherical shell as a result of the inherent emission, absorption, and reflection of thermal energy from its surface can be calculated by use of equation (34). For the purpose of simplifying the computation, the spherical shell is assumed to be at thermal equilibrium with its environment with an isothermal temperature prevailing over the entire surface. Radiation interaction inside the sphere can be assumed to be radially symmetric over the entire surface and producing a uniform pressure outward, and the radiation emitted from the outside is assumed to be radially symmetric over the surface and producing an inward pressure acting against the pressure produced within. The pressure produced on the inner surface can be expressed as

$$p_i = \frac{2\epsilon_i \sigma T^4}{c} \quad (40)$$

where the factor of 2 accounts for the fact that thermal energy is absorbed at the same rate that it is emitted at equilibrium. The uniform and symmetric pressure produced on the outside surface is

$$p_o = \frac{\epsilon_o \sigma T^4}{c} \quad (41)$$



(c) $\theta_c = 80.0^\circ$.

Figure 7.- Concluded.

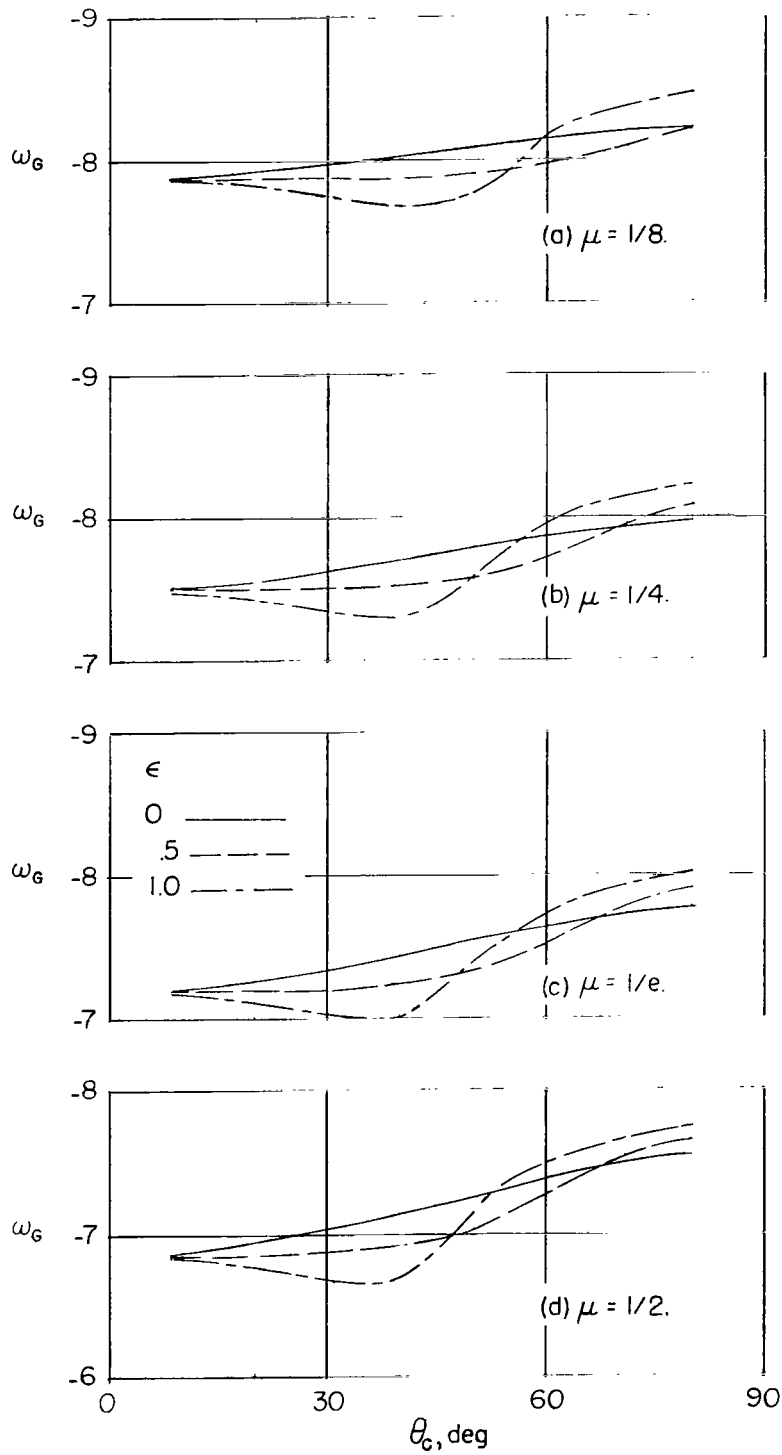


Figure 8.- Location of peak G point. $\frac{WL}{h_s'} = 0.0444$ pound per cubic foot.

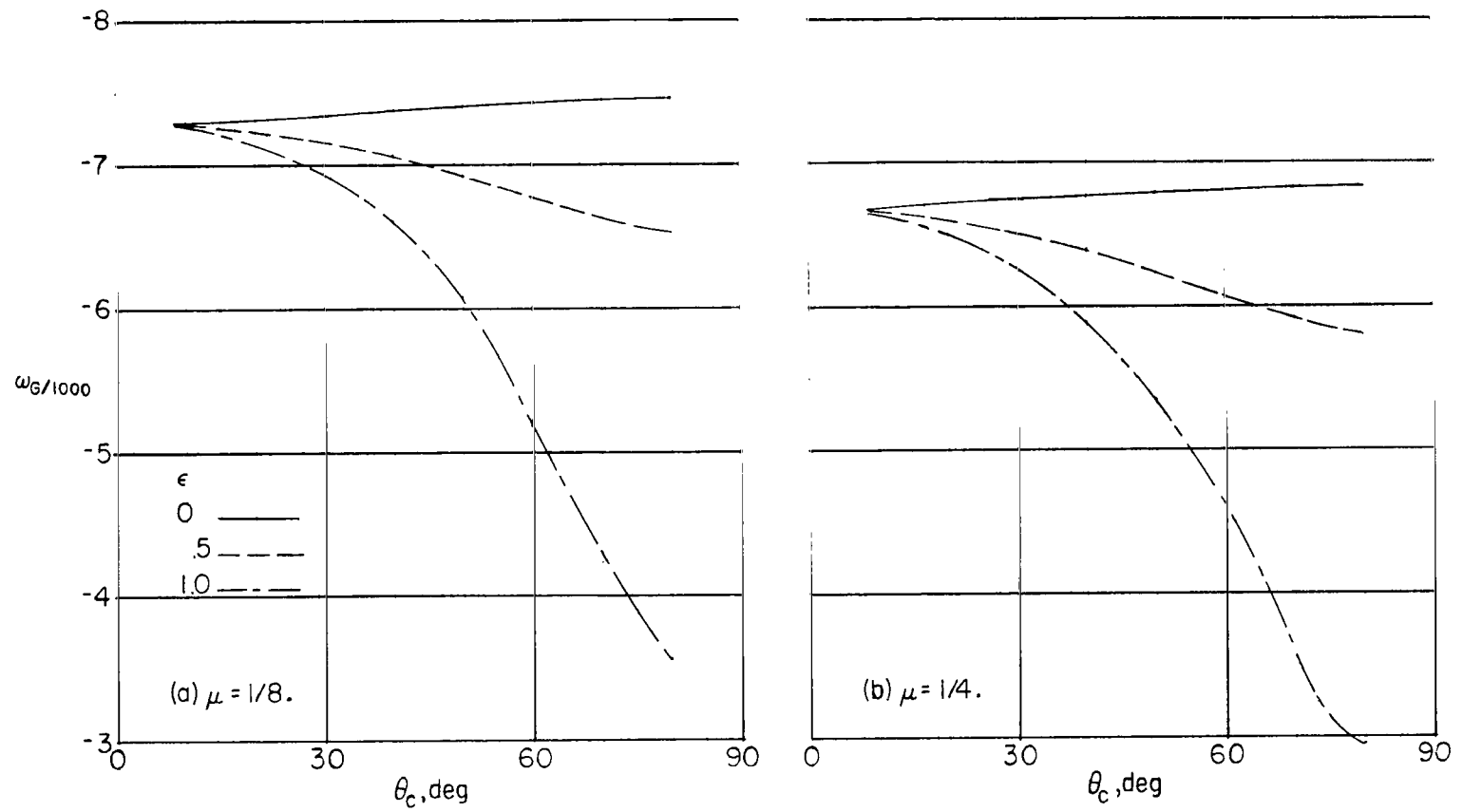


Figure 9.- Location of the low-altitude point of one-thousandth peak G . $\frac{wL}{h_S} = 0.0444$ pound per cubic foot.

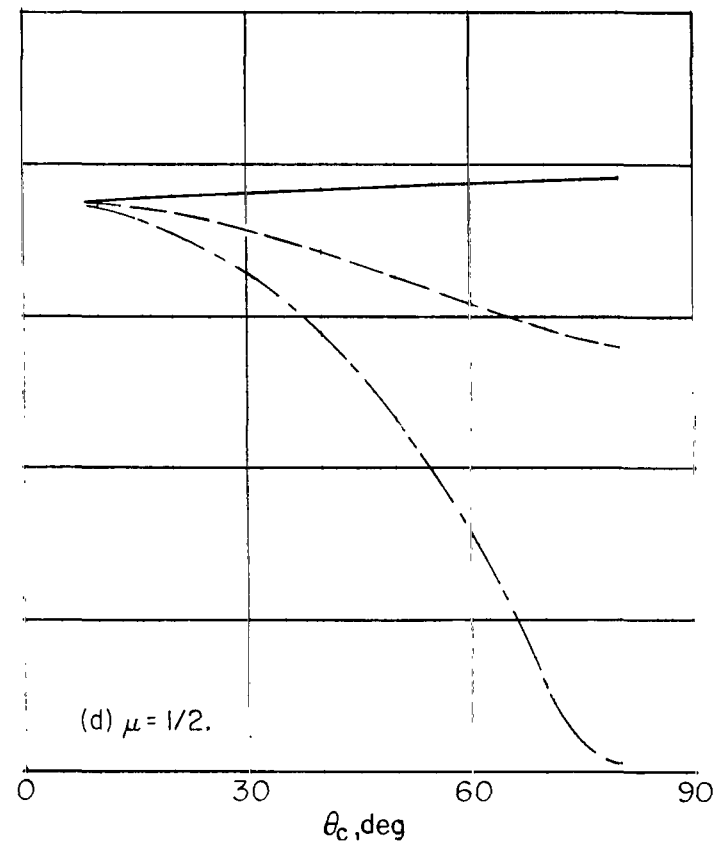
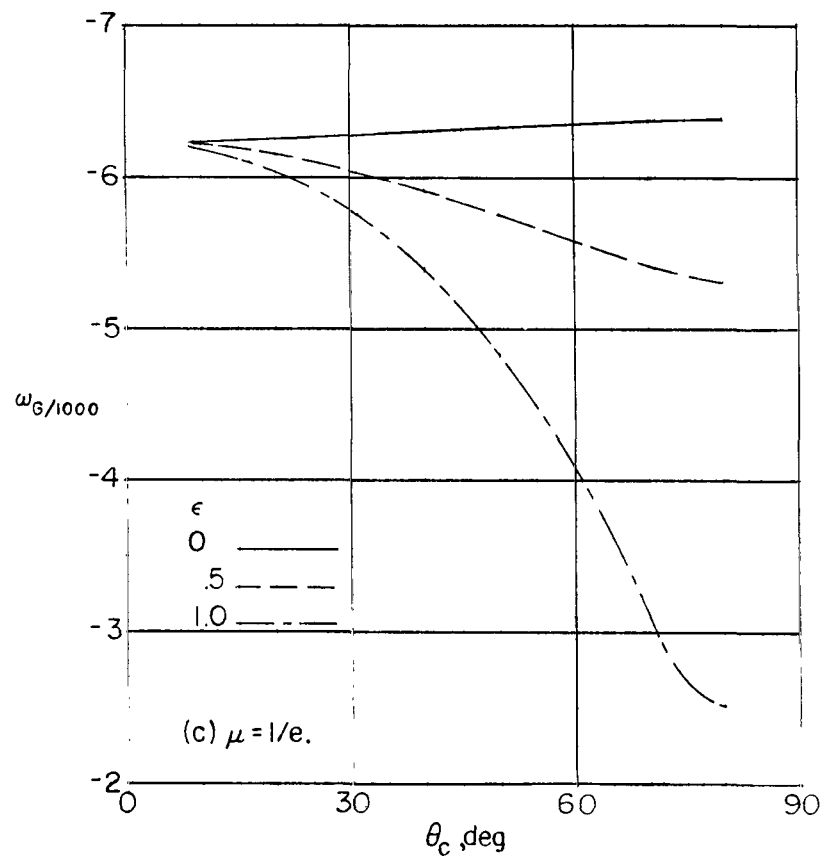


Figure 9.- Concluded.

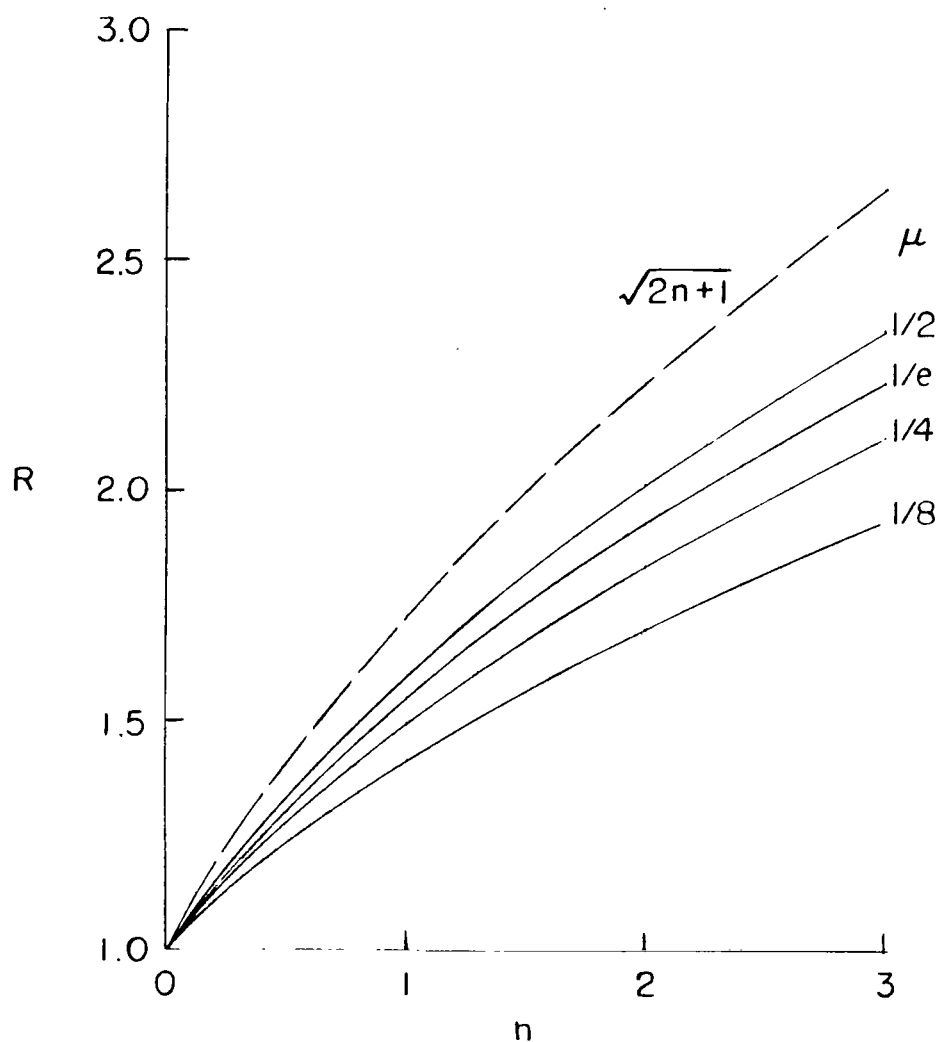


Figure 10.- Limiting velocity of infinitely shallow probes with zero flank loss as a function of the power of the variation of radius with axial distance.